Fusion Engineering and Design 156 (2020) 111602

Contents lists available at ScienceDirect

Fusion Engineering and Design

journal homepage: www.elsevier.com/locate/fusengdes

Interfacial microstructures, residual stress and mechanical analysis of hot isostatic pressing diffusion bonded joint of 93W–4.9Ni–2.1Fe alloy and 30CrMnSiNi2A steel

Wensheng Liu[a], Qingqing Sheng[a], Yunzhu Ma[a], Qingshan Cai[a,*], Jianning Wang[a], Yang Liu[b]

[a] National Key Laboratory of Science and Technology for National Defence on High–strength Structural Materials, Central South University, Changsha, 410083, China
[b] School of Materials Science and Engineering, Hunan University of Science and Technology, Xiangtan, 411201, China

ARTICLE INFO

Keywords:
Tungsten
Steel
Diffusion bonding
Hot isostatic pressing
Residual stress

ABSTRACT

Circular sleeves of 93W–4.9Ni–2.1Fe alloy (W–Ni–Fe) and 30CrMnSiNi2A steel were connected by a hot isostatic pressing (HIP) diffusion bonding method. W–Ni–Fe/steel joint mock–up with a dimension of 30_{ID} mm × 50_{OD} mm × 50_{H} mm was successfully fabricated. Metallographic analysis with field–emission scanning electron microscope (FE–SEM) revealed the diffusion zone of the joint interface consists of W/steel diffusion layer and Ni–Fe/steel diffusion layer. Electron probe microanalysis (EPMA) and X–ray diffraction (XRD) analysis exhibits the brittle intermetallic phase Fe_7W_6 is formed at the W/steel diffusion zone. The average tensile strength of ~310.5 MPa along with 8.6 % elongation has been obtained for the HIP diffusion couple and the fracture occurs predominantly in W–Ni–Fe near the joint interface because of the thermal stress concentration. Thermally induced stresses and strains in the W–Ni–Fe/steel HIP joint were analyzed using finite element method (FEM). The results reveal that the peak equivalent residual stress on entire joint is located at the W–Ni–Fe side near the interface close to the free surface. Meanwhile, the steel substrate releases the residual stress by generating plastic deformation.

1. Introduction

Among all alloyed and unalloyed metals, tungsten (W) has the highest melting point (3410 °C) and lowest vapor pressure (1.3×10^{-7} Pa, at T_{melt}), which makes W and it's alloys are very appropriate for apply in various high–temperature/high–vacuum environment [1]. For its great geometrical stability at elevated temperatures and the highest sputtering threshold of all possible candidates, there is the strongest considerable use as plasma facing materials (PFM) in fusion reactor [2,3]. For the unique combination of properties such as high density (16–18 g/cm^3), hardness of 9.2 GPa, and excellent mechanical strength at elevated temperatures, tungsten alloys are the excellent materials for kinetic energy penetrators (KEP) [4,5].

However, W applications are limited due to high ductile brittle transition temperature (DBTT) (200–500 °C) is associated with irradiation–effected embrittlement, recrystallization embrittlement and poor fabricability [6]. On the other hand, the fabrication of W components with complex shape and large size is difficult and cost. Developing a composite structure of W and the basic structural material steel (e.g. EUROFER97 [7], China low activation martensite (CLAM) steel [8], 30CrMnSiNi2A steel [9]) to substitute full W structure is of great significance. For instance, W/steel connectors are preferred composite structures for divertor components in the DEMO fusion reactor [10–12]. According to the design of the divertor components, W is considered as PFM, and steel is chosen as a heat sink material for its low activation characteristic sufficient resistance against high dose irradiation [13].

The fabrication of W/steel component is a challenging task because of the complicated design of divertor structure for DEMO. According to the design, a W alloy thimble is required to join a steel conic sleeve for use as a finger module component [14,15]. Among the possible methods, diffusion bonding by HIP is accepted as being one of the most suitable methods for the finger structure because it is non–intrusive and isostatic. Thus, the research of the HIP bonding technique on W/steel mock–up part is being carried out.

In this study, a HIP diffusion bonding technique was investigated as a method of joining W–steel joint circular sleeve. The mechanical properties of the joint was measured by tensile testing and the site of fracture was compared to the residual stress distribution estimated by FEM.

* Corresponding author.
E-mail addresses: cai2009pm@163.com, caiqingshan@csu.edu.cn (Q. Cai).

https://doi.org/10.1016/j.fusengdes.2020.111602
Received 13 November 2019; Received in revised form 30 January 2020; Accepted 1 March 2020

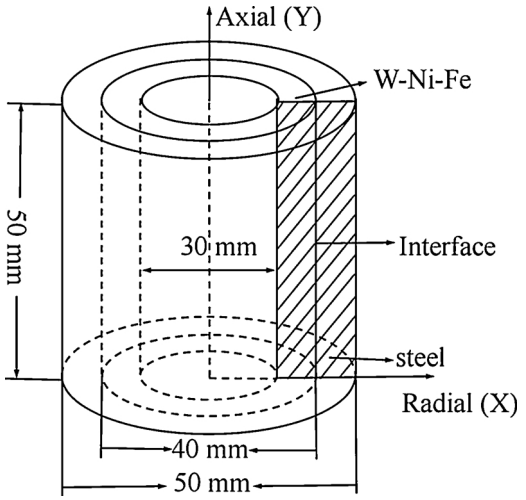

Fig. 1. Combination structure of the sample showing the coordinate system.

2. Experimental procedure and modeling

2.1. Experimental procedure

In this study, Commercially tungsten alloy (W–Ni–Fe, China) and 30CrMnSiNi2A steel (China ultra–high strength low alloy steels) were used as parent materials. The chemical composition of the tungsten alloy is in wt%: 93W, 4.9Ni, 2.1Fe. For the 30CrMnSiNi2A steel, the composition is in wt%: 0.25C, 1.15Si, 1.08Cr, 1.67Ni, 0.27Mo, 0.11V, 0.05Cu, 0.034W, 0.024Al, 0.006Ti, 0.003S, 0.007P, Fe in balance.

Circular sleeves of W–Ni–Fe and steel (30_{ID} mm × 40_{OD} mm × 50_{H} mm for W–Ni–Fe, 41_{ID} mm × 50_{OD} mm × 50_{H} mm for steel) were used for HIP diffusion bonding. Polishing the bonded surfaces of the circular sleeves to a surface roughness R_a of about 1.2 μm by grinder machining. Both W–Ni–Fe and steel circular sleeves were cleaned in ultrasonic bath pot for about 10 min to remove the contaminators on surfaces and get the cleaned bonding surfaces, for HIP diffusion bonding experiment.

Fig. 1 presents the combined structure of W–Ni–Fe/steel, which is enclosed in a 3 mm thick 304 stainless steel can. After exhausting gas for 3 h in vacuum chamber at 500 ℃, the canned materials was out-–gassed to vacuum less than 10^{-3} Pa. The HIP diffusion bonding experiment was conducted at 1050 ℃ with the heating rate of 10 ℃/min. Applying pressure load to 100 MPa uniformly as elevating temperature to 1050 ℃ from room temperature (RT). The HIP temperature of W/steel divertor part should be controlled below 1050 ℃ in order to avoid grain coarsening and phase transition in steel [16]. Then the diffusion bonding process performed at 1050 ℃ for 1 h under the pressure of 100 MPa. Subsequently, the HIP process temperature is cooled down to 400 ℃ from 1050 ℃ at a cooling speed of 5 ℃/min, and then cooling down to RT at a nature cooling speed. At the same time, Relief the pressure load with a uniform speed at cooling process.

Fig. 2 shows a HIP diffusion bonded W–Ni–Fe/steel joint mock–up after removing the canning materials. The cross–section of the bonded joints were cut perpendicularly to the bonding interface and were machined into sub–size specimens by lathe processing and electrical discharge machining (EDM). The microstructure and the various elements distribution across bonding interface between W–Ni–Fe and steel were analyzed using FE–SEM (Novatm Nano SEM230) and EPMA (JXA–8230 F) respectively. The mechanical properties of the bonded specimen were evaluated by hardness and tensile tests. Hardness profile perpendicularly to the bonding interface was determined by Nano–indentation equipped with optical microscope (OM) with a load of 3 mN. Cylindrical specimens with diameter of 2 mm and gauge length of 7 mm are used for the strain controlled tensile tests (stain rate = 0.01 s^{-1}) in universal tensile testing machine (Instron–3369) at RT. The fracture surface of the joint was observed by FE–SEM combine with energy dispersive X–ray spectroscopy (EDS), and analyzed the chemical composition on fracture surface using XRD.

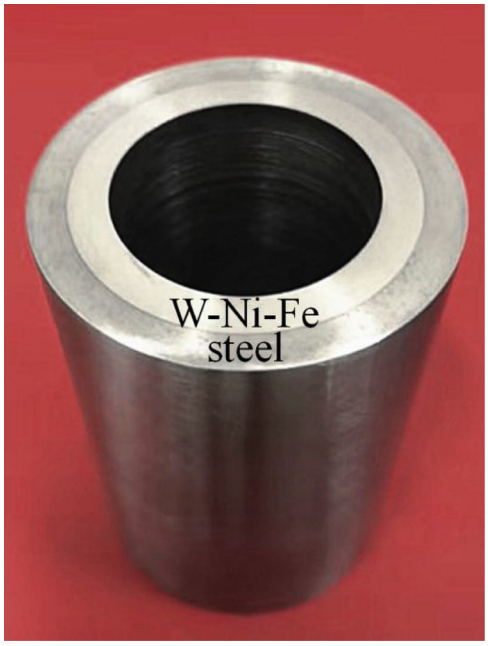

Fig. 2. HIP bonded W–Ni–Fe/steel joint mock–up after removing canning materials.

2.2. Modeling

In this case, a continuum model was established to compute the residual stresses and strains that developed in joining W–Ni–Fe/steel joint as it cooled from a HIP bonding temperature to RT. Considering the symmetry with respect to the y–axis for the bonded sample, a symmetrical stress distribution is assumed. The finite element model was simplified to two dimension planar (radial and axial) for conducting the FEM calculation. The arbitrary meridian plane of four node quadrilateral solid element was established, and the glue operation was applied to treat the bonding interface of the joint. A typically two–dimensional finite element meshing is shown in Fig. 3. Besides, a fine mesh was required in the vicinity of bonding interface and ends for achieving a more accurate result, due to the large stress and strain gradients in this zones. Assuming all materials are isotropic, the temperature–dependent material properties that be required to conduct finite element computation was listed in Table 1, according to the thermomechanical analysis (TMA) experiments. Elastic modulus and Poisson ratio of the materials were measured by high temperature dynamic elastic modulus tester (IET–1600p). Thermal expansion coefficient and yield strength of the materials were measured using thermal expansion coefficient tester (NETZSCH DIL 402 C) and high temperature tensile testing machine (Instron–3369) respectively. Initial condition is set as the diffusion bonding temperature of 1050 ℃ and spatially uniform cooling is assumed. The temperature and pressure function was established for calculation, according to the experimental condition during cooling process.

3. Results and discussion

3.1. Interfacial microstructure

The general SEM–BSE image of cross–section of the W–Ni–Fe/steel joint transition area was presented in Fig. 4, which indicates that the joint is well–bonded and free from crack or discontinuities. In addition,

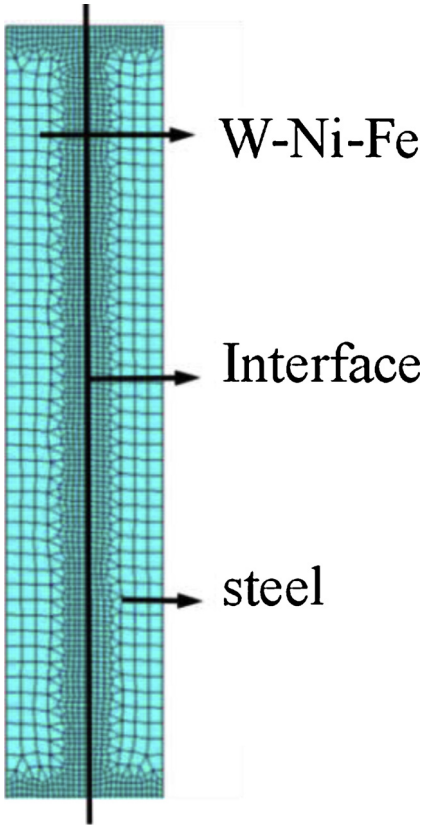

Fig. 3. Typical finite element entire mesh for FEM calculation.

the W–Ni–Fe/steel joint interface area contains two kinds of diffusion region (W/steel and Ni–Fe/steel): W/steel diffusion zone is formed by the connection of W particles in W–Ni–Fe matrix with steel, and Ni–Fe phase in W–Ni–Fe matrix is connected with steel to form Ni–Fe/steel diffusion zone. The higher magnification micrographs showing the detailed microstructures of the two diffusion layers and the corresponding elemental elemental distribution and migration behavior obtained by EPMA analysis are presented in Fig. 5. By the EPMA, a layer of about 3 μm thick was formed in the W/steel diffusion zone. In addition, the elemental concentration distribution is smooth and continuous along the direction normal to bond interface. Meanwhile, neither apparent intermediate phase nor compounds was confirmed because of the microscale of interlayer and the precision limitation of detection. However, a point of elemental concentration with W 49.0 at.% and Fe 50.4 at.% appeared. It can be assumed that this region formed an intermetallic compound of Fe_7W_6, as joining tungsten to steel directly [17]. Fig. 5(d) reveals the diffusion traces of element W, Ni and Fe at the Ni–Fe/steel diffusion zone.

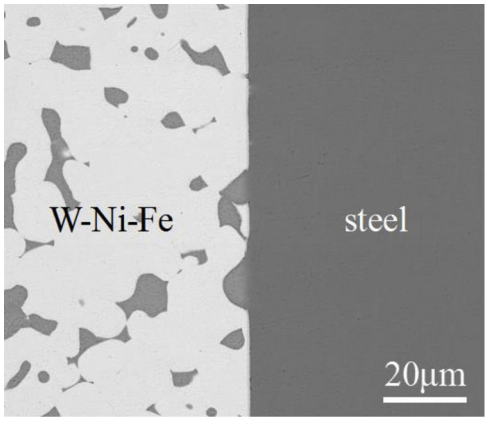

Fig. 4. General SEM–BSE image of cross–section of the W–Ni–Fe/steel joint transition area.

For further investigating the diffusion behavior of elements, the element concentration distribution map was employed to evaluate the diffusion distance and the composition and thickness of diffusion zone formed. Fig. 6 presents EPMA element mapping of W, Ni and Fe taken from the joint transition area. It can be seen that the Ni and Fe concentration in the Ni–Fe phase near the Ni–Fe/steel diffusion layer is different from that in the Ni–Fe phase of the tungsten alloy matrix. In particular, it should be noted that, the Fe concentration was increased and the Ni concentration was decreased in the Ni–Fe phase near Ni–Fe/steel diffusion layer, according to the evidence of Fe penetration into Ni–Fe phase and Ni penetration into steel. Thus, according to the element map (Fig. 6) and diffusion traces (Fig. 5(d)) by the EPMA, the Ni–Fe/steel diffusion zone with a thickness of 5 ~ 8 μm was formed. The two diffusion zones with different thicknesses may lead to a uneven configuration of the joint interface. This corrugated interface could produce a sound and robust interface by preventing the spreading of crack at the joint interface during subsequent mechanical loading. Besides, the presence of Ni–Fe phase on joint interface can reduce the formation of brittle intermetallic phases generated between W and steel [16].

3.2. Mechanical properties

The alteration of micro structure and elemental composition can affect the mechanical properties of materials significantly. For assessing the micro–mechanical properties of W–Ni–Fe/steel bonded interface, the hardness was evaluated across the W/steel and Ni–Fe/steel diffusion layers by Nano–indentation tests. The results are presented in Fig. 7. At the W/steel diffusion layer, the high hardness values (~11.5 GPa) observed in the diffusion zone is associated with the interdiffusion of W and Fe and the possible occurring intermetallic compounds. In the

Table 1
Material properties required in FEM.

Property	Temperature (°C)	Elastic modulus (GPa)	Poisson ratio	Thermal expansion coefficient (10^{-6}/°C^{-1})	Yield strength (MPa)
93W–4.9Ni–2.1Fe alloy	25	361	0.279	4.60	800
	200	355	0.281	4.79	540
	400	346	0.283	5.90	400
	600	337	0.287	5.95	395
	800	324	0.293	6.36	250
	1050	103	0.3	6.68	245
30CrMnSiNi2A steel	25	208	0.281	10.6	505
	200	203	0.290	11.86	460
	400	187	0.294	13.9	450
	600	165	0.313	13.9	260
	800	127	0.322	12.04	94
	1050	99	0.355	12.11	26

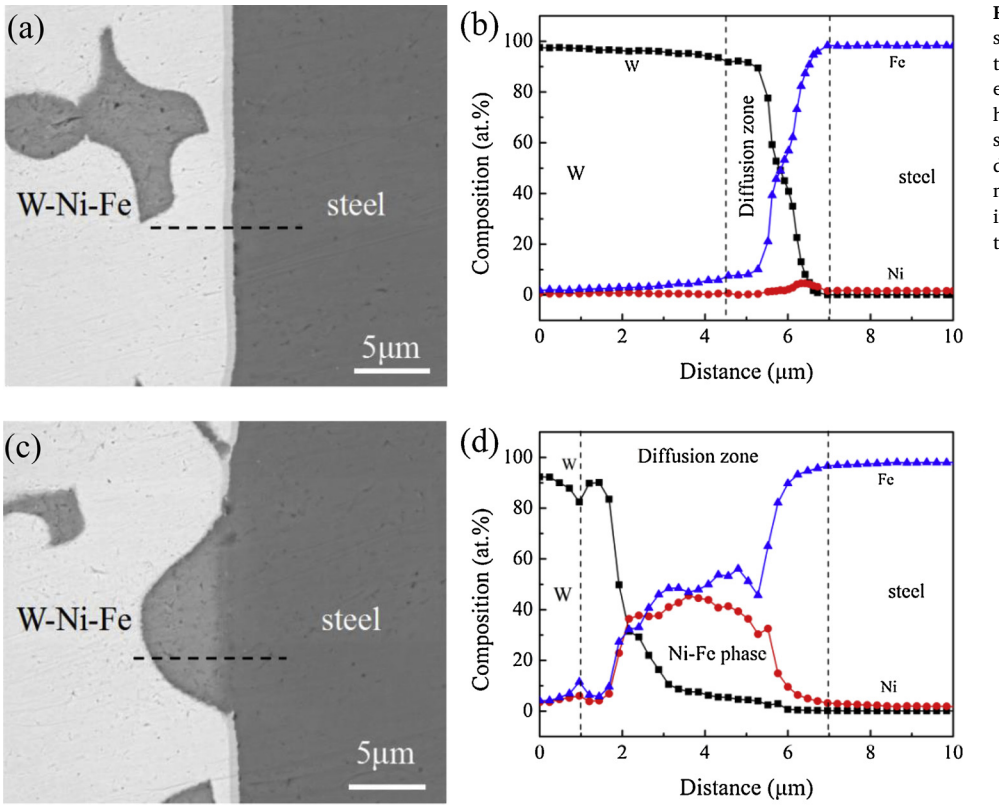

Fig. 5. Higher magnification micrographs showing the detailed microstructures of the two diffusion layers and the corresponding elemental concentration distribution. (a) higher magnification micrograph of the W/steel interface, (b) elemental concentration distribution of the W/steel interface, (c) higher magnification micrograph of the Ni–Fe/steel interface, (d) elemental concentration distribution of the Ni–Fe/steel interface.

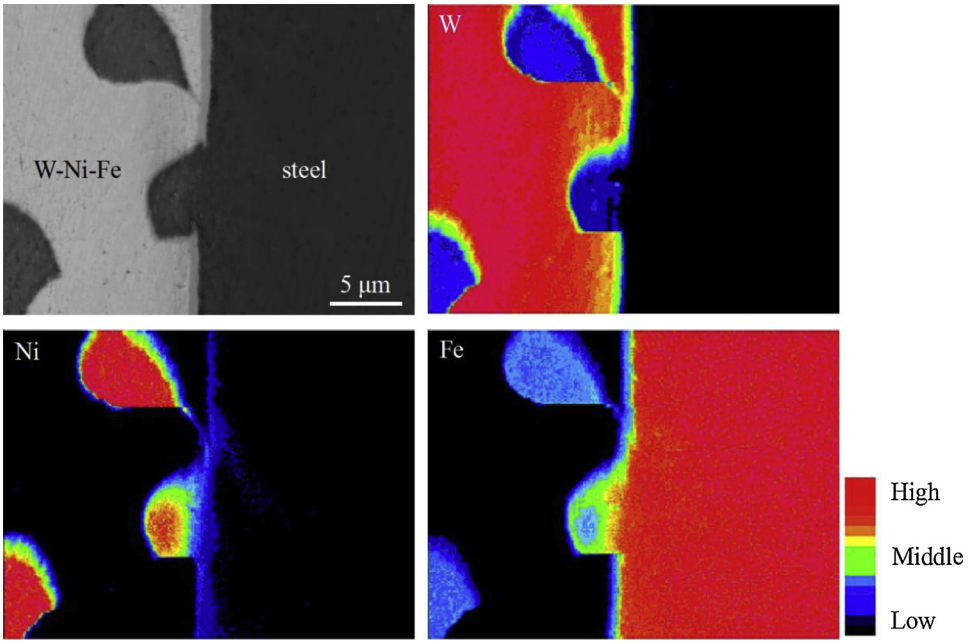

Fig. 6. EPMA element mapping of W, Ni and Fe taken from the joint transition area.

Ni–Fe/steel diffusion layer, similarly, a higher hardness is noted in comparison with the Ni–Fe phase or steel, according to the evidence of Ni or Fe penetration into steel and Fe penetration into Ni–Fe phase. For making a distinguish between the Ni–Fe phase in tungsten alloy matrix and the Ni–Fe phase connected with steel matrix, a hardness value of 4.5 GPa was detected for the Ni–Fe phase in tungsten alloy matrix using Nano–indentation. It should be noted that, compared with the Ni–Fe phase (~4.5 GPa) in the tungsten alloy substrate, the hardness of the Ni–Fe phase (~5.7 GPa) near the Ni–Fe/steel diffusion layer is higher. This may be attributed to large amounts of Fe migration into the Ni–Fe phase (see Fig. 5(d)). Theoretically, Extending diffusion zones and/or reducing brittle intermetallic compounds can achieve a more excellent mechanical properties [18]. This region–dependent hardness is ascribed to the solid solution effect of element interdiffusion and the brittle intermetallic compounds formed by reaction between dissimilar elements. Above results confirmed that the interdiffusion and chemical reaction between different element at interface is being.

The strength and toughness of W–Ni–Fe/steel joint mock–up are of

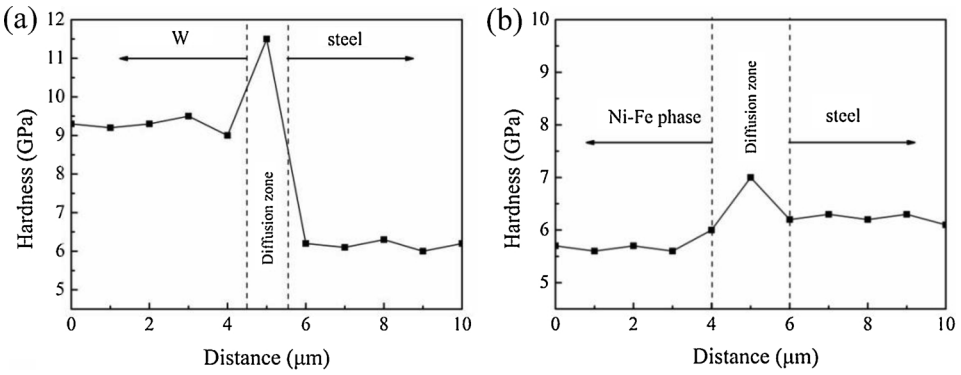

Fig. 7. Hardness distribution along the cross–section of the W–Ni–Fe/steel bonding interface. (a) W/steel interface, (b) Ni–Fe/steel interface.

Table 2
Material properties of the HIP bonded specimen and the base materials before bonding.

	tungsten alloy		Steel		Joint	
	σ_{UTS} (MPa)	δ (%)	σ_{UTS} (MPa)	δ (%)	σ_{UTS} (MPa)	δ (%)
Original	900.1	10.0	773.0	22.5	—	—
HIP	904.9	11.6	1285.9	22.4	310.5	8.6

important for practical applications. The tensile strength σ_{UTS} and the elongation (δ) of the substrates (tungsten alloy and 30CrMnSiNi2A steel) and bonded joint were investigated by tensile tests, and the results are presented in Table 2. The base material properties of tungsten alloy and steel before bonding are also summarized in the table for comparision. After HIP diffusion bonding, the tensile strength and elongation of tungsten alloy are both increased in some extent, which attributed to the elimination of residual pores and more uniform microstructure [19]. However, the change of tensile strength and elongation of 30CrMnSiNi2A steel shows an opposite variation after diffusion bonding. It is worth noting that the tensile strength of 30CrMnSiNi2A steel has sharply increased from 773 MPa to 1285 MPa. This is owing to the transformation of the mixed structure of proeutectoid ferrite and pearlite into the granular bainite structure [20]. The joint strength of ~310.5 MPa along with 8.6 % elongation has been obtained for the HIP bonded mock–up and the fracture predominantly occurs at tungsten alloy matrix near the joint interface during tensile testing, indicating that the joint interface have high bonding properties. As previously reported by W.W. Basuki and J. Aktaa [16], W/steel diffusion bonding specimens with post bonding heat treatment (PBHT) are broken at the bonding seam due to the lower ductility (< 1.5 %). Compared with the W/steel joint prepared by W.W. Basuki and J. Aktaa [16], the W–Ni–Fe/steel joint possessed a higher elongation. The reason can be the presence of the Ni–Fe/steel diffusion zone and the thinner layer of Fe_7W_6 phase at the joint interface.

Meanwhile, from the fracture behavior of W–Ni–Fe side, it was infered that there is a large residual stress developed in the HIP bonded W–Ni–Fe/steel joint during cooling process. For further confirming this assumption, the FEM was employed to investigate the residual stress distribution of the joint.

3.3. Stress and strain distributions

Fig. 8 shows the contour plot of radial and axial stress distribution for the W–Ni–Fe/steel joint, and the higher magnification was given for detail. The negative value in pictures represents compressive stress and the positive value represents tensile stress. Fig. 8(a) shows the contour plot of radial residual stress (σ_x) distribution, which reveals that the value of σ_x is low except for the vicinity of stress singularity, due to the constraint of the small radial shrinkage size. It can be seen from Fig. 8(b), the stress singularity is located at the intersection of the interface and the end. Comparing with steel, the σ_x value in vicinity of the stress singularity is higher at W–Ni–Fe side. Meanwhile, mesh refinement ensured the FEM accuracy near the stress singularity, except for the two elements close to the stress singularity [21]. Fig. 8(c) shows the axial residual stress (σ_y) distribution, indicating that the large σ_y gradient is distributed near the interface. The W–Ni–Fe side is subjected to a axial compressive stress from steel, on the contrary, the tungsten alloy exerts a axial tensile stress to steel. This can be interpreted as that steel with high CET shrank more intense in axial direction than W–Ni–Fe with low CET during cool process. Fig. 8(d) shows that the large axial compressive stress is located at the W–Ni–Fe side near the interface (y = 3 mm to y = 19 mm and y = 31 mm to y = 47 mm), and the great axial tensile stress is mainly distributed in the steel side (y = 12 mm to y = 38 mm).

However, neither σ_x nor σ_y can comprehensively evaluate the effect level of residual stress on mechanical properties of the joint. So we introduced the von Mises equivalent stress (σ_{von}), which can assess the synthesized residual stress of the joint. The contour plot of σ_{von} distribution and the corresponding magnification was presented in Fig. 9, revealing the large σ_{von} is distributed on the W–Ni–Fe side. It can be determined that the residual stress developed in cooling process is much more detrimental for W–Ni–Fe than for steel. Observing Fig. 9(b), the large σ_{von} is mainly located at W–Ni–Fe side near the interface and end of the joint. Meanwhile, there is no large σ_{von} concentration on the steel side, and the σ_{von} distribution is uniform.

The large residual stress is often located near the interface and/or ends. For further knowing the specific magnitude and trends of residual stress in key regions, five locations were selected (y = 0 mm, y = 2 mm, y = 4 mm, y = 6 mm, y = 8 mm) to define paths (path 1, path 2, path 3, path 4, path 5 respectively, see Fig. 9(b). Fig. 9(c) presents the σ_{von} distribution in paths defined along the radial direction in the W–Ni–Fe matrix as a function of distance from the bonding interface. At W–Ni–Fe side, the σ_{von} distribution confirmed that the residual stress near the interface and end is largest. It was noted that the peak σ_{von} 808 MPa is located on path 1 about distancing 1 mm from the interface. Besides, these zones with large stress concentration became the weak regions and are prone to failure. Although there is no large residual stress distribution on the W–Ni–Fe/steel interface, it is also a weak zone due to the presence of bonding defects and/or reaction productions like brittle intermediate phases which are prone to rupture and promote micro crack propagation.

Fig. 10 given the contour plot of von Mises equivalent plastic strain (ε_{von}) distribution and the corresponding magnification. The ε_{von} can comprehensively evaluate the plastic deformation generated in W–Ni–Fe/steel joint during cooling process. From Fig. 10(a), there is relatively large ε_{von} on the steel side near the interface, which can reduce the residual stress in steel matrix. Because compared with tungsten, steel with low yield strength can accommodate extensive localized plasticity without generating high residual stresses [21,22]. It can be

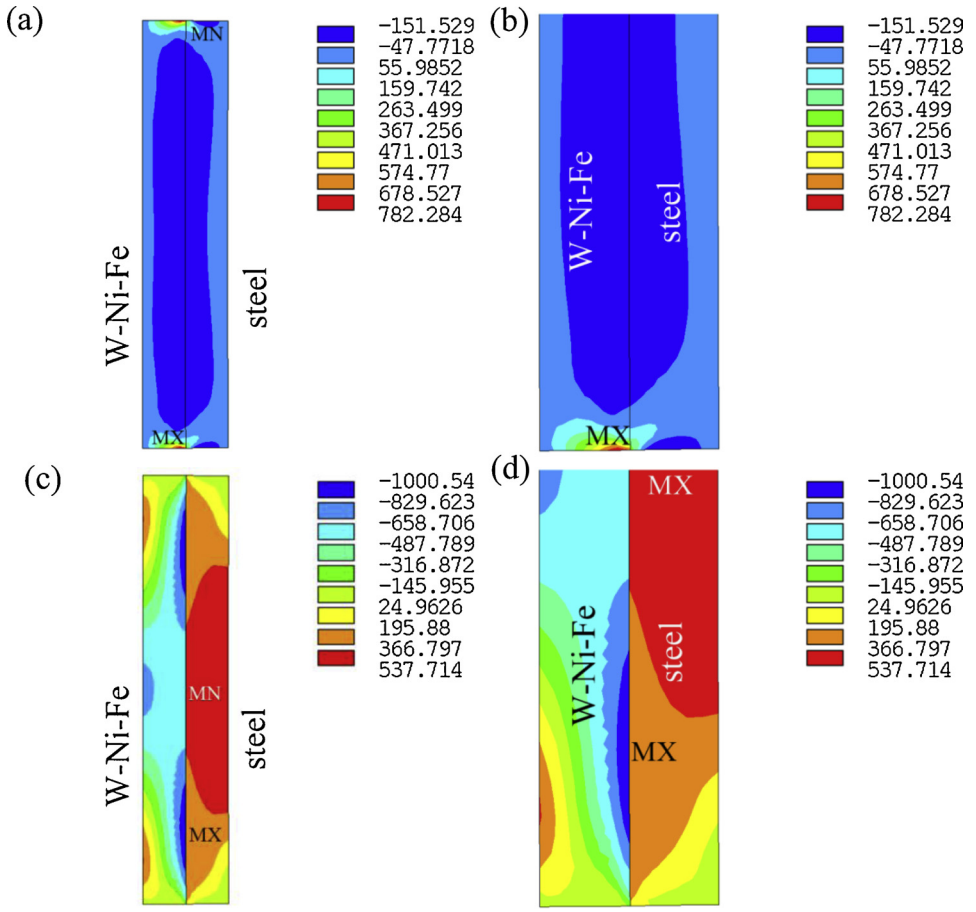

Fig. 8. Contour plots of the residual stress distribution for the W–Ni–Fe/steel joint. (a) axial stress σ_x (in MPa), (b) high magnification of the axial stress σ_x (in MPa), (c) radial stress σ_y (in MPa), (d) high magnification of the radial stress σ_y (in MPa).

seen from Figs. 10(b) and 9 (b) that the maximum ε_{von} in steel side faced the maximum σ_{von} located at W–Ni–Fe side. This confirmed that the steel can reduced residual stress and avoid large stress concentration by generating plastic deformation. Once the steel suffered a large stress, it would produce plastic deformation to release the stress and maintain the residual stress stable. This also explains why the distribution of σ_{von} on the steel side is uniform, while the value of ε_{von} varies in these region.

3.4. Fracture characteristics

The typical fracture surface on W–Ni–Fe side of W–Ni–Fe/steel joint was given in Fig. 11, which reveals that the fracture is macroscopically divided into region I and region II. Region I is determined as the torn–off W characterized by faceted grains through the analysis of FE–SEM and EDS. As shown in Fig. 11(a), the fraction of W that remained on the fracture surface is the major part. It can be inferred that the failure is mainly due to the large thermal residual stress formed in tungsten alloy matrix near the joint interface during cooling process. Fig. 11(b) presents the higher magnification fractured surfaces of region II, revealing that the region consists of area A and area B. The area A on fracture surface was identified as containing Fe (~95 at.%) by EDS, suggesting the area A is the steel matrix. While area B is comprised of W (~49 at.%) and Fe (~50 at.%), it can be expected as the brittle intermetallic compound Fe_7W_6. For further confirming the fracture behavior, the fracture surface was detected by XRD and the result was given in Fig. 12, the presence of Fe_7W_6 phase was confirmed. According above results, the fracture mode can be described as that the crack initial in W–Ni–Fe side near the joint interface due to the thermal residual stress concentration, then the crack propagated rapidly along the W grain boundaries and partly into brittle intermetallic phase. In some zones, because of the thin diffusion layer, the crack entered the steel through the brittle intermetallic compound Fe_7W_6. The above results revealed that the simulation results are consistent with experimental results, and also verified the correctness of simulation. On the base of the discovery that thermal stress cause to be factor of crack, the next work will focus on investigating the effect of post bonding heat treatment (PBHT) on the properties of joint.

4. Conclusions

W–Ni–Fe/steel joint mock–up with sound bonding interface and good mechanical properties was fabricated by HIP. Through analyzing and generalizing the results of simulation and experiment, some conclusions were drawn as following:

(1) Good bonding at the interface and a lack of micro–cracks was inferred from the microstructural analysis. The joint strength of ~310.5 MPa along with 8.6 % elongation has been obtained by tensile tests.
(2) The large residual stress mainly concentrated on the vicinity of bonding interface and end. The peak σ_{von} is located in W–Ni–Fe side near the bonding interface. The plastic deformation is produced on the steel side, which helps to released the thermal residual stress of steel.
(3) Fracture mainly occur in W–Ni–Fe side near the interface. The fracture behavior was determined as the crack initial in W grains, and partly into brittle intermetallic phase and steel. Meanwhile, it

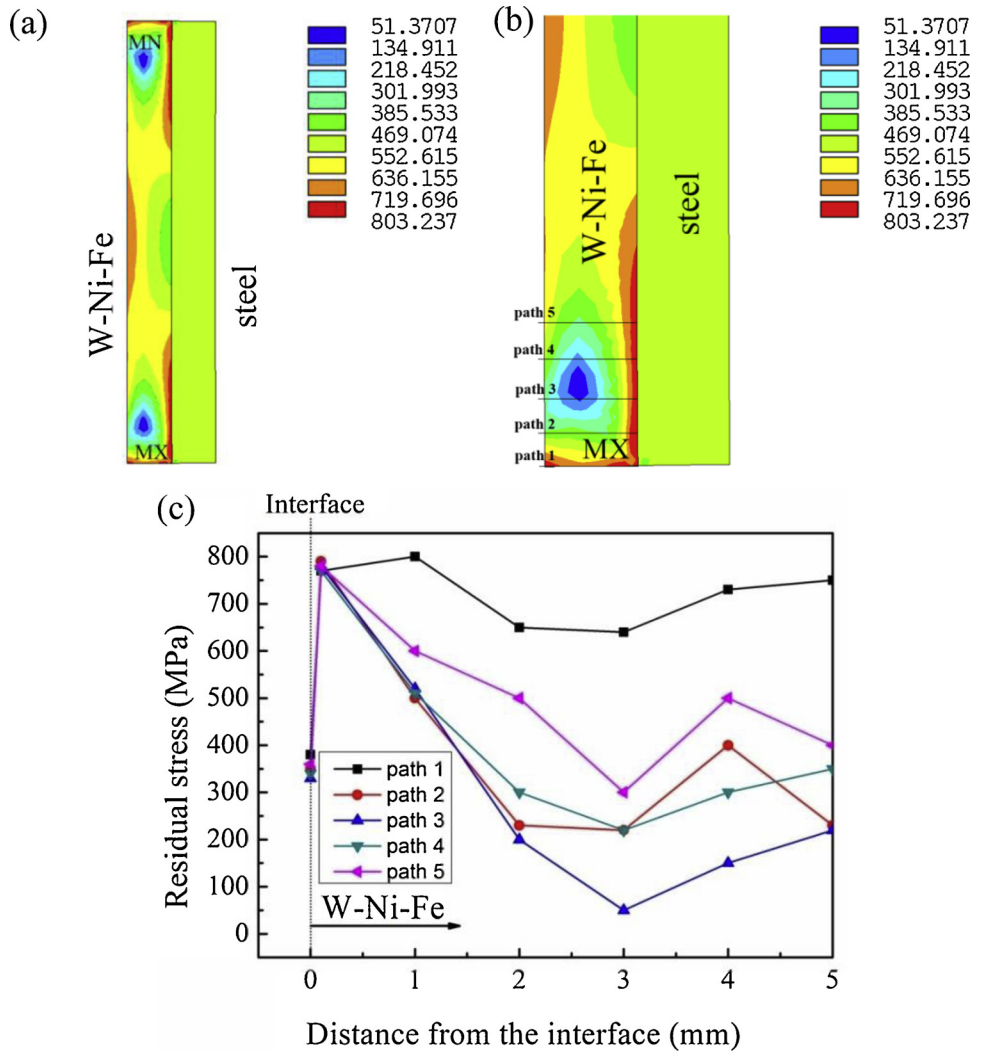

Fig. 9. Contour plots of the residual stress distribution for the W–Ni–Fe/steel joint and the stress profile. (a) von Mises equivalent stress σ_{von} (in MPa), (b) high magnification of the von Mises equivalent stress σ_{von} (in MPa), (c) von Mises equivalent stress σ_{von} profiles along the radial direction in W–Ni–Fe substrate as a function of distance from the joining interface.

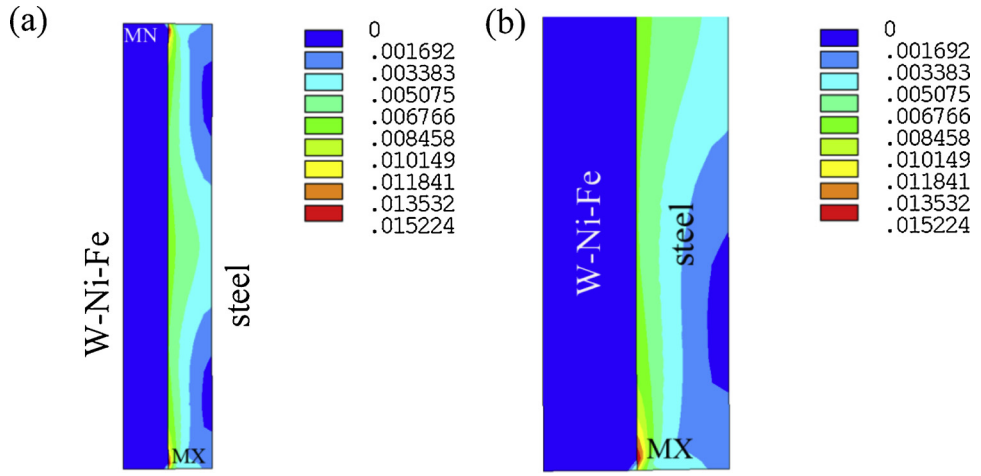

Fig. 10. Contour plots of the residual strain distribution for the W–Ni–Fe/steel joint, (a) von Mises equivalent strain ε_{von} (in mm), (b) high magnification of the von Mises equivalent stain ε_{von} (in mm).

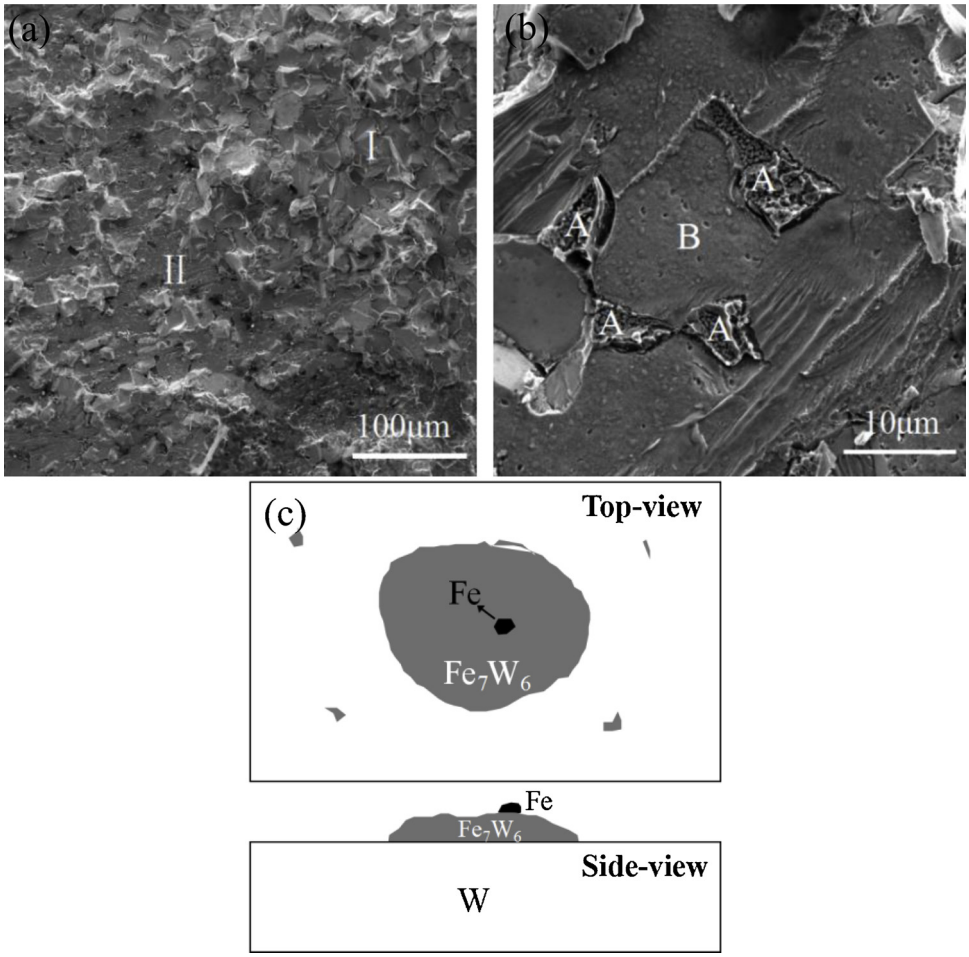

Fig. 11. Fracture surface of the W–Ni–Fe/steel joint after tensile test. (a) representative fractured surface, (b) fracture surface of region II. (c) schematic of fracture morphology.

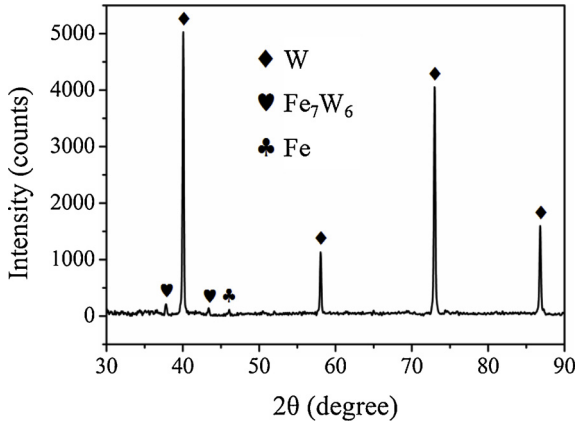

Fig. 12. XRD result on the tensile fracture surface.

was be drawn that experimental results is consistent with simulation results.

Credit author statement

I have made substantial contributions to the conception or design of the work; or the acquisition, analysis, or interpretation of data for the work.

I have drafted the work or revised it critically for important intellectual content and I have approved the final version to be published.

I agree to be accountable for all aspects of the work in ensuring that questions related to the accuracy or integrity of any part of the work are appropriately investigated and resolved.

All persons who have made significant contributions to the work reported in the manuscript, including those who provided editing and writing assistance but who are not authors, are named in the Acknowledgments section of the manuscript and have given their written permission to be named. If the manuscript does not include Acknowledgments, it is because the authors have not received substantial contributions from nonauthors.

Declaration of Competing Interest

None.

Acknowledgments

This work was supported by the National Natural Science Foundation of China (Grant nos. 51701242, 51931012), and the Natural Science Foundation of Hunan Province of China (Grant no. 2018JJ3648).

References

[1] I. Smid, M. Akiba, G. Vieider, L. Plöchl, Development of tungsten armor and bonding to copper for plasma–interactive components, J. Nucl. Mater. 258–263 (1998) 160–172.

[2] R. Neua, H. Maier, M. Balden, S. Elgeti, H. Gietl, H. Greuner, A. Herrmann, A. Houben, V. Rohde, B. Sieglin, I. Zammuto, ASDEX Upgrade Team, Investigations

on tungsten heavy alloys for use as plasma facing material, Fusion Eng. Des. 124 (2017) 450–454.
[3] A. Terra, G. Sergienko, M. Tokar, D. Borodin, T. Dittmar, A. Huber, A. Kreter, Y. Martynova, S. Möller, M. Rasiński, M. Wirtz, Th. Loewenhoff, D. Dorow–Gerspach, Y. Yuan, S. Brezinsek, B. Unterberg, Ch. Linsmeier, Micro–structured tungsten: an advanced plasma–facing material, Nucl. Mater. Energy. 19 (2019) 7–12.
[4] A. Kumari, M. Sankaranarayana, T.K. Nandy, On structure property correlation in high strength tungsten heavy alloys, Int. J. Refract. Met. Hard Mater. 67 (2017) 18–31.
[5] R. Luo, D. Huang, M. Yang, E. Tang, M. Wang, L. He, Penetrating performance and "self–sharpening" behavior of fine–grained tungsten heavy alloy rod penetrators, Mater. Sci. Eng. A 675 (2016) 262–270.
[6] W.W. Basuki, R. Dahm, J. Aktaa, Thermomechanical analysis of diffusion–bonded tungsten/EUROFER97 with a vanadium interlayer, J. Nucl. Mater. 455 (2014) 635–639.
[7] W.W. Basuki, J. Aktaa, Investigation of tungsten/EUROFER97 diffusion bonding using Nb interlayer, Fusion Eng. Des. 86 (2011) 2585–2588.
[8] C. Zhang, H. Li, M. Li, Role of surface finish on interface grain boundary migration in vacuum diffusion bonding, Vacuum 137 (2017) 49–55.
[9] Z. Chu, G. Zhou, Q. Yang, K. Wang, T. Min, J. Wang, Study of the robust earth penetrator penetrating concrete target, Explo. Shock Waves 24 (2004) 115–121.
[10] M. Koller, A. Kruisova, R. Mušálek, J. Matějíček, H. Seiner, M. Landa, On the relation between microstructure and elastic constants of tungsten/steel composites fabricated by spark plasma sintering, Fusion Eng. Des. 133 (2018) 51–58.
[11] J.B. Wang, Y.Y. Lian, F. Feng, Z. Chen, Y. Tan, S. Yang, X. Liu, J.B. Qiang, T.Z. Liu, M.Y. Wei, Y.M. Wang, Microstructure of the tungsten and reduced activation ferritic–martensitic steel joint brazed with an Fe–based amorphous alloy, Fusion Eng. Des. 138 (2019) 164–169.
[12] J.C. Wang, W. Wang, R. Wei, X. Wang, Z. Sun, C. Xie, Q. Li, G.N. Luo, Effect of Ti interlayer on the bonding quality of W and steel HIP joint, J. Nucl. Mater. 485 (2017) 8–14.
[13] T. Weber, J. Aktaa, Numerical assessment of functionally graded tungsten/steel joints for divertor applications, Fusion Eng. Des. 86 (2011) 220–226.
[14] M.J. Kruszewski, Ł. Ciupiński, M. Rosiński, A. Michalski, K.J. Kurzydłowski, Pulse plasma sintering of a tungsten/steel divertor module, Fusion Eng. Des. 88 (2013) 2573–2576.
[15] H.Y. Chen, L.M. Luo, J. Zhang, X. Zan, X.Y. Zhu, G.N. Luo, Y.C. Wu, Investigation on W/Fe diffusion bonding using Ti foil and Ti powder interlayer by SPS, J. Nucl. Mater. 467 (2015) 566–571.
[16] W.W. Basuki, J. Aktaa, Investigation on the diffusion bonding of tungsten and EUROFER97, J. Nucl. Mater. 417 (2011) 524–527.
[17] K. Martin, K. Alena, M. Radek, M. Jiří, S. Hanuš, L. Michal, On the relation between microstructure and elastic constants of tungsten/steel composites fabricated by spark plasma sintering, Fusion Eng. Des. 133 (2018) 51–58.
[18] T. Chehtov, J. Aktaa, O. Kraft, Mechanical characterization and modeling of brazed EUROFER–tungsten–joints, J. Nucl. Mater. 367–370 (2007) 1228–1232.
[19] U. Engel, Heinz Hübner, Strength improvement of cemented carbides by hot isostatic pressing (HIP), J. Journal of Materials Science. 13 (1978) 2003–2012.
[20] W.S. Liu, X.K. Pang, Y.Z. Ma, Q.S. Cai, Development of fully dense and high performance powder metallurgy HSLA steel using HIP method, Mater. Res. Express 5 (2018) 312–317.
[21] R.L. Williamson, B.H. Rabin, G.E. Byerly, FEM study of the effects of interlayers and creep in reducing residual stresses and strains in ceramic–metal joints, Compos. Eng. 5 (1995) 851–863.
[22] M.H. Yu, B. Zhou, D.B. Bi, D. Shaw, Preparation of graded multilayer materials and evaluation of residual stresses, Mater. Design. 31 (2010) 2478–2482.